



In situ observations of phase transition between perovskite and CaIrO₃-type phase in MgSiO₃ and pyrolitic mantle composition

Shigeaki Ono^{a,*}, Artem R. Oganov^b

^a*Institute for Research on Earth Evolution, Japan Agency for Marine-Earth Science and Technology, 2-15 Natsushima-cho, Yokosuka-shi, Kanagawa 237-0061, Japan*

^b*Laboratory of Crystallography, Department of Materials, ETH Hönggerberg, Wolfgang-Pauli-Strasse 10, CH-8093 Zurich, Switzerland*

Received 26 October 2004; received in revised form 19 March 2005; accepted 1 June 2005

Available online 14 July 2005

Editor: B. Wood

Abstract

In situ observations of the perovskite–CaIrO₃ phase transition in MgSiO₃ and in pyrolitic compositions were carried out using a laser-heated diamond anvil cell interfaced with a synchrotron radiation source. For pure MgSiO₃, the phase boundary between the orthorhombic Mg-perovskite and CaIrO₃-type phases in the temperature range of 1300–3100 K was determined to be P (GPa) = $130 (\pm 3) + 0.0070 (\pm 0.0030) \times (T - 2500)$ (K) using platinum as a pressure calibrant. We confirmed that the CaIrO₃-type phase remained stable up to pressures of at least 156 GPa and temperatures of 2600 K. The consistency of our results with previous theoretical calculations leads us to conclude that the 2700 km seismic discontinuity at the bottom of the lower mantle can be attributed to a phase transition to the CaIrO₃-type phase. The phase change from an orthorhombic Mg-perovskite to a CaIrO₃-type bearing assemblage in a pyrolitic mantle composition was also observed at $P = 125$ GPa, which corresponds to the same mantle depth as the seismic discontinuity. The phase boundary between the orthorhombic Mg-perovskite and CaIrO₃-type bearing assemblage was determined to be P (GPa) = $124 (\pm 4) + 0.008 (\pm 0.005) \times (T - 2500)$ (K) using gold as a pressure calibrant. This transition boundary indicates that the temperature at a depth of 2700 km is about 2600 K, and the adiabatic temperature gradient in the lower mantle is estimated to be 0.31 K/km. The partition coefficients and the effect of some elements on the phase equilibrium between the orthorhombic MgSiO₃ perovskite and CaIrO₃-type MgSiO₃ were estimated from ab initio calculations. Our experimental and theoretical results indicate that the D'' layer consists of a CaIrO₃-type bearing assemblage which is likely to have significant effect on the chemical and thermal evolution of the Earth's mantle.

© 2005 Elsevier B.V. All rights reserved.

Keywords: CaIrO₃-type phase; phase transition; MgSiO₃; peridotite; D'' layer

* Corresponding author. Tel.: +81 46 867 9763; fax: +81 46 867 9625.

E-mail address: sono@jamstec.go.jp (S. Ono).

1. Introduction

From seismic observations, it is well known that a boundary between the solid silicate mantle and the liquid iron core (CMB) exists at a depth of 2900 km. Recent seismic studies have shown that the region above the CMB, called the D'' layer, contains strong seismic anomalies. The seismic discontinuity, anisotropy, and an anticorrelation between the observed shear and bulk sound velocities have been reported [e.g., [1–8]]. Many researchers have tried to explain these seismic properties at the D'' layer using various models, such as phase transitions, partial melt, chemical heterogeneity, mineralogical anisotropy, and small-scale convection [e.g., [9–13]]. Recently, anomalies in the electrical conductivity at the base of the lower mantle have also been observed [e.g., [14,15]]. Mineralogists have expended enormous effort to solve these enigmas. From the viewpoint of mineralogy and petrology, the Earth's lower mantle is believed to be composed mainly of Fe- and Al-bearing Mg-perovskite, which has an orthorhombic symmetry. Many experimental studies have indicated that orthorhombic Mg-perovskite of both pure and natural mantle compositions is stable at pressures corresponding to those found in the lower part of the lower mantle [e.g., [16–22]]. In contrast, a post-perovskite phase transition was reported in iron oxide, Fe_2O_3 [23]. It is known that a large amount of Fe_2O_3 can be dissolved in MgSiO_3 perovskite [24,25]. Ono et al. [23] observed that Fe_2O_3 , like MgSiO_3 , transforms from the corundum (ilmenite) structure to the perovskite (or $\text{Rh}_2\text{O}_3(\text{II})$) structure under pressure. An analogous phase transition seems to contribute to the high solubility of Fe_2O_3 in MgSiO_3 perovskite. Moreover, on further compression above pressures of 60 GPa, a new post-perovskite type Fe_2O_3 phase with an orthorhombic ($Cmcm$) CaIrO_3 -type structure, becomes stable [26]. Therefore, the same structure seemed to be likely stable for MgSiO_3 at high pressures. Recently, this pioneering idea was confirmed by theoretical and experimental studies [27–30]. The transition depth from the orthorhombic Mg-perovskite to the CaIrO_3 -type phase matched that of the observed seismic discontinuity at the D'' layer [27]. Using ab initio calculations, previous studies [27,28] reported the Clapeyron slope of this transition to be 8–10 MPa/K, a value that is not constrained by the experimental

study. In natural mantle compositions, orthorhombic Mg-perovskite and CaIrO_3 -type phases are likely to contain other components, such as FeO, Fe_2O_3 , and Al_2O_3 , and the effect of impurities on the transition pressure is unknown.

In this study, we used a double-sided laser heated diamond anvil cell (DAC) that was subjected to intense X-rays from a synchrotron radiation source at SPring-8 facility in Japan, which made it possible to acquire precise data on a sample under high pressures and high temperatures. We report on the results of in situ X-ray observations of the phase boundary between orthorhombic perovskite and the CaIrO_3 -type phase in MgSiO_3 and KLB-1 peridotite, which have similar compositions to pyrolite. We also investigated the effect of impurities on the transition pressure, and we discuss the relationship between the phase boundary determined by our experiments and the seismic observations of the discontinuity at the D'' layer.

2. Methods

2.1. High-pressure experiments

Enstatite and synthetic gel powder were used as the starting materials in the MgSiO_3 experiments. In the case of the natural mantle composition experiments, only synthetic gel was used. The chemical composition of this gel was similar to KLB-1 peridotite, and the composition was confirmed using XRF analysis (Table 1). High-pressure X-ray diffraction experiments were performed using a double-sided laser heating diamond anvil cell (DAC) system. A symmetric-type diamond cell (SYNTEC Co. Ltd., Japan) with 60° conical apertures was used [31]. Cubic boron

Table 1
Comparison of chemical compositions of pyrolite, KLB-1 peridotite, and the starting material

	Pyrolite	KLB-1	SM
SiO_2 (wt.%)	46.1	44.8	45.5
TiO_2	0.2	0.2	0.2
Al_2O_3	4.3	3.6	3.3
FeO^a	8.2	8.2	8.2
MgO	37.6	39.5	38.3
CaO	3.1	3.5	3.6
Na_2O	0.4	0.3	0.3

^a All iron has been calculated as FeO.

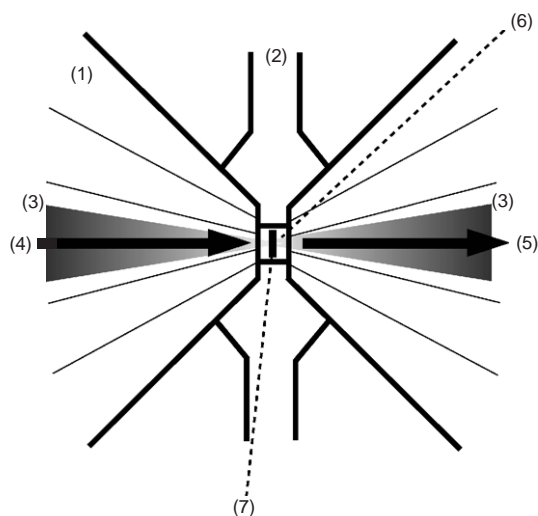


Fig. 1. Schematic illustration of the high pressure–temperature X-ray diffraction system. (1) diamonds, (2) Re gasket, (3) YLF or YAG lasers, (4) incident X-ray, (5) diffracted X-ray, (6) argon pressure transmitting medium, (7) sample.

nitride seats were used in the DAC because of the hardness of CBN, and its X-ray transparency, which allowed for a large opening angle for the scattered X-rays. Fig. 1 is a schematic drawing of the experimental set-up. The synthetic powdered sample was loaded into a 50–100 μm diameter hole that was drilled into a rhenium gasket using an excimer laser. The sample powder was mixed with platinum or gold powder, used as an internal pressure calibrant. These powders were mechanically ground in an agate mortar for several hours to ensure homogeneity and a small grain size. The volume fractions of platinum and gold employed in our study were higher than those used in the conventional DAC experiments. Therefore, the diffraction peaks of platinum or gold were more intense than those of the sample or the argon pressure transmitting medium. These intense platinum and gold peaks allowed for reliable pressure determination. The sample was pressed into a disc to a thickness of less than 15 μm . Argon was cryogenically loaded into the sample chamber, acting as a pressure transmitting and thermally insulating medium. The argon reduced any deviatoric stress and temperature gradients occurring across the sample. No pressure transmitting medium was used in the KLB-1 peridotite experiments, because the intensity of the X-ray diffraction patterns was weak and good quality

data could not be acquired. The samples were heated using the TEM₀₁-mode of a YLF laser or multi-mode YAG laser to overcome any potential kinetic effects on the possible phase transitions. The size of the laser spot was 20–30 and 50–100 μm for the YLF and YAG lasers, respectively. But the size of the high-temperature region was smaller than that of the laser spot. Examples of typical temperature profiles are shown in Fig. 2. The laser beam was not scanned to heat the sample, because scanning leads to the complicated temperature history during the heating, and thus promotes inhomogeneity of the chemical equilibrium in the sample. The sample temperature was measured using the spectroradiometric method [21,32]. The spectroradiometric data collection system consisted of a thermoelectrically cooled CCD detector (Princeton Instruments, HAM 256x1024, USA) and a spectrograph (Acton Research, SpectraPro-150, USA). The spectrometer allowed us to measure the temperature profile across the laser-heated spot. The entrance slit of the spectrograph is used to select a thin line that

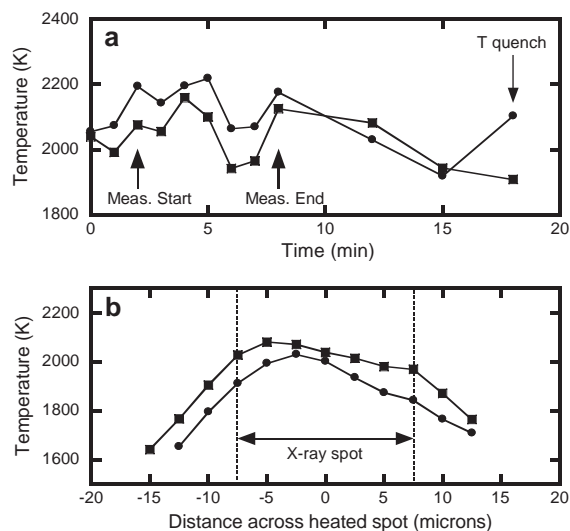


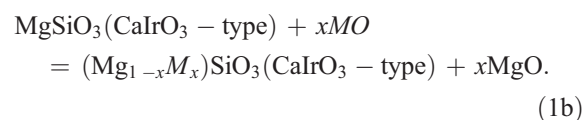
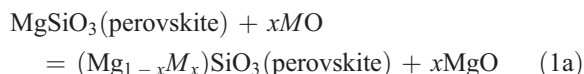
Fig. 2. Examples of temperature fluctuation and profiles during laser heating for KLB-1 peridotite sample. a, Plotted temperatures were obtained at the center of X-ray beam during the heating with the constant laser power. Temperatures were measured at both sides of the sample. X-ray diffraction data was acquired from 2 to 8 min after the desired temperature achieved. After being kept at the desired pressure and temperature for the desired duration, the sample was quenched by cutting off the laser power supply. b, Examples of temperature profiles with the YAG laser for KLB-1 peridotite were measured from both sides of the sample.

traverses the laser spot. A temperature profile across the hotspot was measured at 2.5 μm step. To accurately adjust the center of the heated spot in the entrance slit of the spectrograph, the small pinhole reference was put in the sample holder before experiments. The image of the pinhole was monitored by the spectrograph. According to this image, we could set the pinhole position at the optimum entrance slit position, and then, the laser beam could be aligned with the sample in the optimum entrance slit position using the photograph of the sample. The temperature was determined by fitting the thermal radiation spectrum between 600 and 800 nm to the Planck radiation function. When the difference between the reference of grey body spectrum and the spectrum from the sample is large, the temperature estimation is not reliable. Therefore, we adopted only calculated temperatures which show that the correlation factor between the ideal and the observed spectrums was higher than 80%. The system response was calibrated using a tungsten ribbon lamp (OL550, Optronic Laboratories, USA) with known radiance, and the temperature uncertainty was within 30 K. The pressure was determined from the observed unit cell volumes of platinum or gold using the known equations of state of platinum or gold. The uncertainty in the pressure value is related to the experiment temperature because of the use of the EOS for platinum or gold. The samples were probed using an angle-dispersive X-ray diffraction technique at the synchrotron beam line at the BL10XU, SPring-8 [26,32]. A monochromatic incident X-ray beam with a wavelength of $\lambda \sim 0.42 \text{ \AA}$ was used. The X-ray beams were collimated to a diameter of 10–20 μm , and the angle-dispersive X-ray diffraction patterns were obtained on an online imaging plate (Rigaku, Japan) or X-ray CCD detector (Bruker, Germany). The sample positioning and laser beam alignment can be done precisely as follows. First, we set the DAC on the stage, and adjusted the sample position into focus of the CCD monitors. Next, using the DAC positioning system, we adjusted the sample position to the X-ray beam position precisely. We monitored the X-ray beam intensity distribution transmitted through the DAC by scanning the DAC. The shape of the sample and the gasket hole were reflected in the obtained two-dimensional map of the transmitted X-ray intensity, by which we could set the sample on the X-ray beam position. The pre-

cision of the relative sample position to the X-ray beam was within 5 μm . Finally, we made refinements of laser beam focus and its position toward the adjusted sample position [26]. The observed intensities on the imaging plates were integrated as a function of 2θ using the ESRF Fit2d code [33] to obtain conventional, one-dimensional diffraction profiles.

2.2. Computational methodology

We have explored the incorporation of divalent impurities ($M = \text{Fe}^{2+}$, Ca^{2+} , Sr^{2+} , Ba^{2+} , and Be^{2+}) into the perovskite- and CaIrO_3 -type phases of MgSiO_3 by comparing the enthalpies of the following reactions at a pressure of 120 GPa:



The enthalpy difference between these reactions is directly related to the partition coefficient of M^{2+} between the two MgSiO_3 phases ($K \approx \exp_B^{-\Delta H/k_B T}$). To calculate these enthalpy differences (ΔH), one needs the enthalpies of the pure and M^{2+} -doped MgSiO_3 phases, which were calculated using large 160-atom supercells ($4 \times 1 \times 2$ for the CaIrO_3 -type post-perovskite, $2 \times 2 \times 2$ for the perovskite phase), using the Γ -point for Brillouin zone sampling, a 600 eV plane-wave cut-off and a 2400 eV cut-off for the augmentation charges. Calculations were performed within the generalized gradient approximation (GGA, [34]) using the all-electron PAW method [35,36] as implemented in the VASP code [37]. The PAW potentials had [He] core (radius = 1.52 a.u.) for O, [Ne] core (1.5 a.u.) for Si, [Be] core (2.0 a.u.) for Mg, [He] core (1.8 a.u.) for Be, [Ne] core (2.3 a.u.) for Ca, [Ar]3d¹⁰ core (2.5 a.u.) for Sr, [Kr]4d¹⁰ core for Ba (2.8 a.u.), [Ar] core (2.3 a.u.) for Ni, [Ne]3s² core (2.2 a.u.) for Fe. Both magnetic and non-magnetic states were studied for the Ni^{2+} and Fe^{2+} impurities, and in all cases, the magnetic (high-spin) states were preferred at pressures of 120 GPa. The results are summarized in Table 2.

Table 2

Energetics of incorporation of divalent impurities and coupled Al–Al substitutions into perovskite- and CaIrO₃-structured phases of MgSiO₃ at 120 GPa

Cation	ΔH_{pref} , eV	$K_{\text{pv-ppv}}$
Be ²⁺	0.821	0.092
Ca ²⁺	0.154	0.64
Sr ²⁺	0.925	0.068
Ba ²⁺	2.271	0.0014
Ni ²⁺	0.397	0.32
Fe ²⁺	−0.239	2.00
Al ³⁺ –Al ³⁺	0.286	0.44

Positive values of ΔH_{pref} indicate better solubility in perovskite. The uncertainty of ΔH_{pref} is about 10%. Partition coefficients at 4000 K are given.

Our ab initio molecular dynamics simulations were performed using the NVT -ensemble [38] for five different volumes (corresponding to static pressures of 0, 40, 80, 120, and 160 GPa) at temperatures of 1000, 3000 and 5000 K. We used 120-atom supercells ($3 \times 1 \times 2$), a time step of 1 fs, a plane-wave cut-off of 500 eV, and the Γ -point for Brillouin zone sampling; and the simulations were run for at least 1.58 ps after equilibration. The Grüneisen parameter $\gamma(V)$ was calculated as in previous studies [39–41] and was accurately represented by the following function [42,43]:

$$\gamma = \gamma_{\infty} + (\gamma_0 - \gamma_{\infty}) \left(\frac{V}{V_0} \right)^{\beta}, \quad (2)$$

where γ_0 (1.553), γ_{∞} (1.114), and β (4.731) are fitted parameters, and V_0 (167.67 Å³) was a reference volume (chosen as the theoretical or experimental zero-pressure volume). An analogous fit for orthorhombic Mg-perovskite [40,41] resulted in $\gamma_0=1.506$, $\gamma_{\infty}=1.14821$, $\beta=7.02469$, $V_0=162.40$ Å³.

By combining the static equation of state [27] with the calculated value of $\gamma(V)$, we were able to determine the classical Mie–Grüneisen thermal equation of state that is valid at high temperatures in the D'' layer.

$$P(V, T) = P_{\text{st}}(V) + \gamma(V) \frac{3nRT}{V}. \quad (3)$$

To counteract any errors in the GGA calculations, we applied a constant pressure shift of −11.2 GPa to all the calculated equations of state. The pressure correction was taken from Oganov et al. [40], and it takes into account the small difference between the

static equations of state of perovskite reported in Oganov et al. [40] and in this present work (these differences result from a different treatment of the valence wave functions close to atomic nuclei). The calculated thermoelastic parameters are listed in Table 3.

3. Results

3.1. MgSiO₃

In the first set of experiments, a powdered MgSiO₃ enstatite starting material mixed with plati-

Table 3

Theoretically predicted physical properties of CaIrO₃-type phase of MgSiO₃ and CaIrO₃-type phase bearing assemblage of KLB-1 peridotite

MgSiO ₃			
High- T Birch–Murnaghan EOS at 2500 K			
$V_{2500.0}$ (Å)	175.097		
$K_{2500.0}$ (GPa)	166.911		
$K'_{2500.0}$	4.473		
$(dK_T/dT)_P$ (GPa K ^{−1})	−0.0414		
$(dK'_T/dT)_P$ (K ^{−1})	0.000318		
Thermal expansion ^a	a	b	c
	(10 ^{−5} K ^{−1})	(10 ^{−10} K ^{−2})	(10 ^{−12} K ^{−3})
At 0 GPa	3.07	0	3.86
At 130 GPa	1.17	3.09	0
KLB-1 peridotite			
Density jump ^b	a	b	
$\Delta\rho$ (%)	1.064	−21.5×10 ^{−6}	
Temperature jump ^c	ΔT (K)		
	40–50		
Temperatures ^d in the lower mantle (K)			
660 km depth	1973		
2700 km depth	2600		
Adiabatic temperature gradient (K/km)			
660 km < depth <	0.31		
2700 km			

^a Thermal expansion is represented as $\alpha = a + bT + cT^2$. These results were obtained within the classical approximation valid above the Debye temperature (~1500 K), i.e., at all conditions of the D'' layer.

^b Density jump along the phase boundary; $\Delta\rho$ (%) = $a + bT$ (K). The volume fraction of Fe- and Al-bearing MgSiO₃ phase is assumed as 75%.

^c Temperature jump is estimated using thermodynamic data [27].

^d Estimated temperatures were determined by high-pressure experimental constraints based on the seismic discontinuities. 660 km depth, Ito and Katsura [73]; 2700 km depth, this study.

num was used. The pressure was increased directly to about 100 GPa at room temperature, and an X-ray diffraction pattern of the sample was recorded. No MgSiO_3 or argon peaks could be identified, and only broad platinum X-ray diffraction peaks were observed. This indicated that a strain-broadening of the diffraction peaks had occurred, which was the result of large differential stresses that were induced in the diamond anvil cell experiments as the pressure increased. After the desired pressure was achieved, the sample was heated to relax the differential stress

and to overcome potential kinetic effects on possible phase transitions. During heating, new diffraction peaks appeared in the diffraction patterns at $P=113$ GPa and $T=1700$ K (Fig. 3a). Most of the new diffraction peaks were reasonably indexed to the orthorhombic perovskite structure ($Pbnm$). However, some peaks did not belong to the orthorhombic MgSiO_3 perovskite structure. These unassigned peaks remain on decompression to ambient pressure. These peaks exhibited a different pressure shift from those of the MgSiO_3 phase. The lowest diffracted

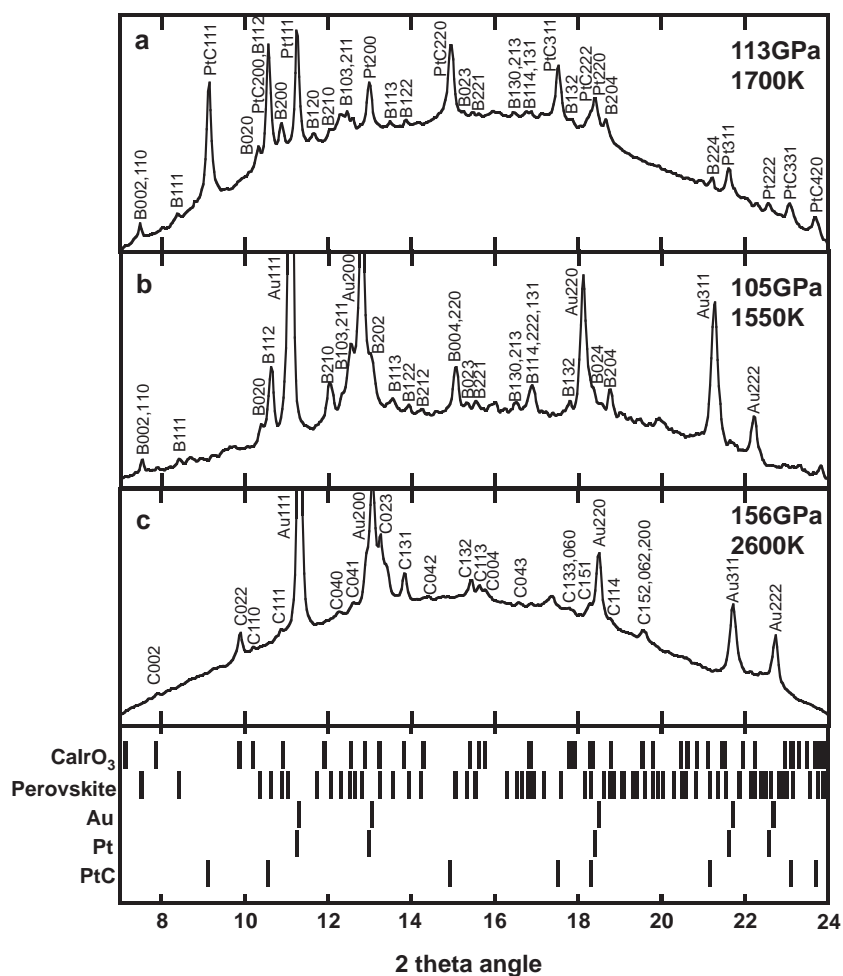


Fig. 3. Examples of observed X-ray diffraction patterns of high pressure forms in MgSiO_3 . a, orthorhombic perovskite phase ($Pbnm$) at 113 GPa and 1700 K; b, orthorhombic perovskite phase ($Pbnm$) at 105 GPa and 1550 K; c, CaIrO_3 -type phase ($Cmcm$) at 156 GPa and 2600 K. In bottom figure, vertical bars indicate the calculated positions of the diffraction lines of each phase. The sample was mixed with platinum powder in only Fig. 2a. In other runs, the sample was mixed with gold powder. Abbreviations of peak labels are as follows: B, orthorhombic perovskite; C, CaIrO_3 -type phase; Pt, platinum; Au, gold; PtC, platinum carbide.

Table 4
Experimental results for MgSiO₃

<i>P</i> (GPa)	<i>T</i> (K)	Result	<i>P</i> (GPa)	<i>T</i> (K)	Result
112.5(1.4)	1900(200)	A	129.9(1.4)	1510(200)	B
113.3(1.5)	2130(220)	A	129.9(1.5)	2090(210)	B
114.6(1.4)	2190(200)	A	130.4(1.4)	1660(200)	B
115.7(1.5)	2520(220)	A	130.4(1.4)	1830(200)	B
117.2(1.5)	2300(210)	A	130.5(1.5)	1750(210)	B
118.9(1.4)	2240(210)	A	130.5(1.4)	1940(200)	B
119.9(1.4)	2060(200)	A	130.7(1.4)	1620(200)	B
120.1(1.4)	2570(200)	A	131.2(1.4)	1860(200)	B
120.9(1.4)	2770(200)	A	131.2(1.9)	2210(270)	B
121.3(1.4)	2620(200)	A	131.3(1.4)	1620(200)	B
121.7(1.4)	2520(200)	A	131.5(1.7)	1740(240)	B
123.0(1.5)	2930(220)	A	131.5(1.4)	1870(200)	B
126.1(1.5)	1600(210)	B	131.6(1.4)	1890(200)	B
127.2(1.4)	2360(200)	A	131.9(1.4)	1720(200)	B
127.4(1.4)	1970(200)	B	132.0(1.5)	1780(210)	B
127.3(1.4)	2070(200)	B	132.3(1.4)	2770(200)	B
127.8(1.4)	1820(200)	B	132.4(1.4)	1570(200)	B
128.6(1.5)	2780(220)	A	132.4(1.4)	1620(210)	B
128.8(1.4)	1620(200)	B	133.0(1.7)	2030(240)	B
129.0(1.4)	1890(200)	B	133.3(1.5)	2360(220)	B
129.2(1.8)	3100(260)	A	133.3(1.6)	3350(230)	A

Abbreviations are as follows: A, orthorhombic perovskite phase; B, CaIrO₃-type phase.

angle of the unassigned peaks was $2\theta=9.14^\circ$ ($d=2.60$ Å). This has also been reported by Shim et al. [30,44]. They concluded that the appearance of this peak indicated a phase transition from the MgSiO₃ perovskite structure to a new high-pressure phase. In our experiments, we could identify several peaks from the unassigned phase in addition to the 2.60 Å peak. Same unassigned peaks have also been reported at higher pressures coexisting with the peaks from the CaIrO₃-type MgSiO₃ phase [27]. Although Shim et al. [30,44] claimed that the unassigned peaks belonged to a new high-pressure MgSiO₃ phase, our results show that these unassigned peaks are not related to MgSiO₃. To verify our proposition, we performed additional runs under different experimental conditions. In our additional experiments, we replaced the platinum calibrant with gold, and did not use any argon pressure transmitting medium. Fig. 3b shows the diffraction pattern of these new experiments. The unassigned peaks did not appear at $P=105$ GPa and $T=1550$ K, corresponding to the orthorhombic perovskite stability field. Moreover, we performed experiments at higher pressures using the gold pressure standard

at $P=156$ GPa and $T=2600$ K, which corresponds to the CaIrO₃-type phase stability field. Fig. 3c shows that unassigned peaks disappeared in the CaIrO₃-type phase stability field. These results indicate that unassigned peaks were somehow related to platinum, because argon is chemically stable. The unassigned peaks were reasonably well indexed to a cubic symmetry with an NaCl-type structure. The bulk modulus, K_0 , of the NaCl-type phase at 0 GPa was about 300 GPa [31], which is much higher than that of MgSiO₃ perovskite (~260 GPa) reported in previous studies [e.g., [19,45]]. The unit cell parameter at ambient pressure and temperature was $a=4.813$ Å. Many metal carbides exhibit the NaCl-type structure with a similar cell parameter [e.g., [46]]. Therefore, the unassigned peaks were assigned to platinum carbide (PtC). During laser heating, platinum mixed with the sample was therefore likely to react with the carbon on the surface of the diamond anvils.

A similar heating method using argon pressure transmitting medium was used in the other runs. Our results for the orthorhombic perovskite and CaIrO₃-type stability regions are summarized in Table 4 and Fig. 4. The dP/dT slope of the phase boundary was

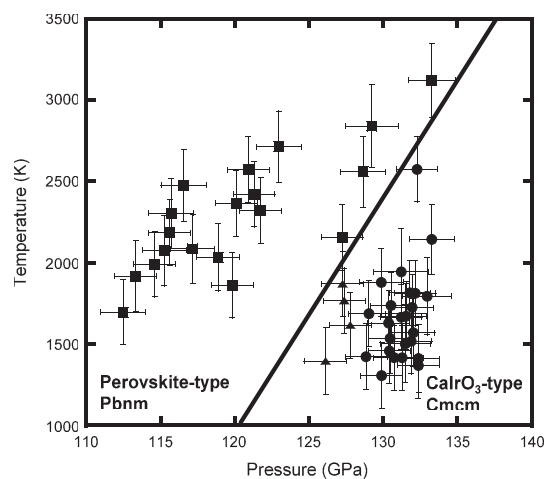


Fig. 4. Experimental results of in situ X-ray observation using the equation of state of platinum. Solid circles and squares represent conditions where orthorhombic perovskite and CaIrO₃-type phase, respectively, were stable. Solid triangles are from Oganov and Ono [27]. Thick line is the inferred phase boundary between orthorhombic perovskite and CaIrO₃-type phases in MgSiO₃.

positive. The transition boundary shown in Fig. 4 is represented by the linear equation

$$P(\text{GPa}) = 130(\pm 3) + 0.0070(\pm 0.0030) \\ \times (T - 2500)(\text{K})$$

based on the equation of state (EOS) of platinum [47]. When the electronic thermal pressure correction of the EOS of platinum [48] was used, the boundary shifted about 1 GPa to the high-pressure side. In contrast, using other EOS for platinum [49] moved that the boundary to lower pressures than that of Holmes's EOS. The difference in pressure between the equation of state by Holmes et al. [47] and that of Jamieson et al. [49] was about 4 GPa.

3.2. KLB-1 peridotite

Experiments for the KLB-1 peridotite composition, which is similar to pyrolite, were conducted at pressures of 108 to 130 GPa and temperatures of 1700 to 2600 K. The pressure was calculated using the EOS

for gold [49]. In the first run, the pressure was increased directly to 97 GPa, and the sample was then heated while the X-ray diffraction patterns were recorded (Fig. 5). Typical heating durations employed were 10–20 min. During heating, the pressure increased to 108 GPa at 1900 K. This pressure increase was likely to have been due to thermal expansion, because the volume of the gold had nearly the same value both before and during heating. The KLB-1 peridotite composition sample crystallized into an assemblage of orthorhombic Mg-perovskite+cubic Ca-perovskite+ferropericalse. This result is in close agreement with those of previous quench experiments using both multi-anvil presses and DACs [e.g., [18,50,51]]. However, diffraction peaks of ferropericalse were ambiguous, because diffraction peaks of orthorhombic Mg-perovskite interfered with those of ferropericalse. Then, the sample was compressed again and heated to 2400–2600 K. The orthorhombic Mg-perovskite remained stable up to 123 GPa and 2600 K. In a second set of experiments, the sample was compressed to around 105 GPa and then heated to

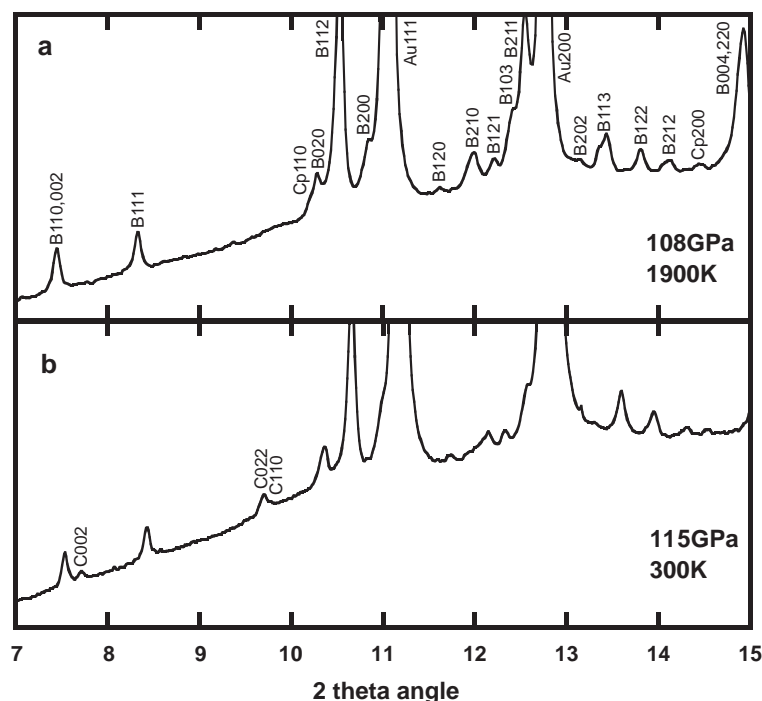


Fig. 5. Examples of observed X-ray diffraction patterns of KLB-1 peridotite. a, Fe- and Al-bearing perovskite assemblage at 108 GPa and 1900 K; b, CaIrO_3 -type phase bearing assemblage at 115 GPa and 300 K after the heating. Abbreviations of peak labels are as follows: B, Fe- and Al-bearing perovskite; C, CaIrO_3 -type phase; Cp, cubic Ca-perovskite; Au, gold.

2050 K. The X-ray diffraction patterns showed that an orthorhombic Mg-perovskite bearing assemblage was present. Then, the sample was compressed and heated to 120 GPa and 1700 K. We observed new peaks, which indicated that the CaIrO_3 -type phase, appeared from the KLB-1 peridotite composition. The same heating method was performed in other heating cycles. The CaIrO_3 -type phase assemblage remained stable up to 130 GPa and 2500 K.

Our results for the orthorhombic perovskite and CaIrO_3 -type stability regions using the KLB-1 peridotite composition are shown in Table 5 and Fig. 6. The value of dP/dT slope of the phase boundary was about 8 MPa/K. The transition boundary shown in Fig. 6 is represented by the linear equation

$$P(\text{GPa}) = 124(\pm 4) + 0.008(\pm 0.005) \\ \times (T - 2500)(\text{K})$$

based on the equation of state (EOS) of gold [49]. Assuming the average depth of discontinuities above the D'' layer to 2700 km, which corresponds to a pressure of 125 GPa, the phase transition from the orthorhombic Mg-perovskite-to CaIrO_3 -type phase bearing assemblage is likely to occur at 2600 K. It is known that the difference between the EOS for gold reported by previous studies is not negligible [e.g., [52,53]]. Experimental pressures based on EOS of gold by Anderson et al. [54] and Shim et al. [55] are several GPa lower than those using Jamieson's. In contrast, Tsuchiya's EOS of gold [56] is several GPa higher than Jamieson's EOS. Pressures based

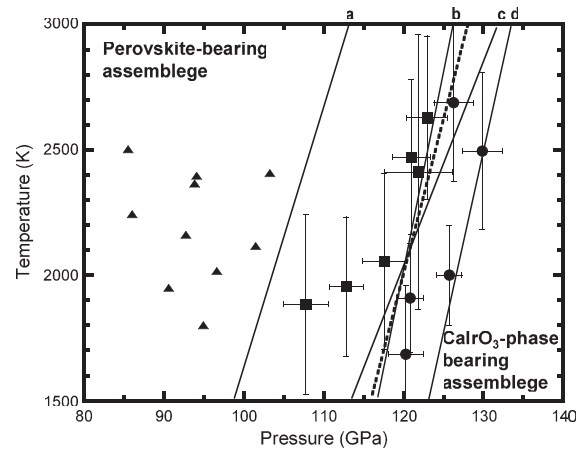


Fig. 6. Experimental results of in situ X-ray observation using the equation of state of gold. Solid squares and circles represent conditions where Fe- and Al-bearing Mg-perovskite assemblage and CaIrO_3 -type phase bearing assemblage, respectively, were stable. Solid triangles are from Ono et al. [21]. Dashed line represents phase boundary between Fe- and Al-bearing Mg-perovskite and CaIrO_3 -type phase bearing assemblages in KLB-1 peridotite. Thick lines are as follows: a, LDA calculation [27]; b, seismic observations [4]; c, GGA calculation [27]; d, experimental results of pure MgSiO_3 in this study. The inferred phase boundary between orthorhombic perovskite and CaIrO_3 -type phases in MgSiO_3 .

on Heinz's EOS [57] generally agree with those based on Jamieson's EOS. To fix the phase change from the orthorhombic Mg-perovskite-to the CaIrO_3 -type phase bearing assemblage at the lowermost part of the lower mantle, it is therefore necessary to improve the experimental method to address the above problems.

4. Discussion

Although it is widely believed that the Earth's lower mantle is composed of an orthorhombic Fe- and Al-bearing Mg-perovskite dominated assemblage, our results indicate that the CaIrO_3 -type phase bearing assemblage exists at the base of lower mantle (i.e., D'' layer). Fig. 7 shows a schematic drawing of the mineral constitution of the Earth's mantle. According to previous multi-anvil experiments [e.g., [50,58,59]], it is recognized that Mg_2SiO_4 polymorphs, such as olivine, wadsleyite, and ringwoodite, are major constituents of the upper mantle and the transition zone. The mineral assemblage of the lower mantle seems to

Table 5
Experimental results for KLB-1 peridotite

P (GPa)	T (K)	Result
107.8(2.8)	1880(360)	A
112.8(2.2)	1950(280)	A
117.6(2.8)	2050(350)	A
120.3(2.2)	1680(280)	B
120.8(1.7)	1910(220)	B
121.0(2.4)	2470(310)	A
121.9(4.3)	2410(550)	A
123.0(2.6)	2630(330)	A
125.8(1.6)	2000(200)	B
126.3(2.5)	2690(310)	B
129.9(2.5)	2490(310)	B

Abbreviations are as follows: A, orthorhombic perovskite bearing assemblage; B, CaIrO_3 -type bearing assemblage.

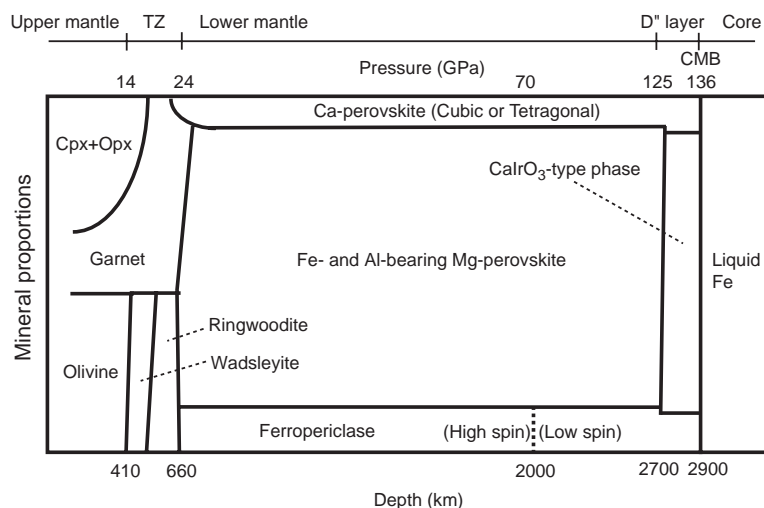


Fig. 7. Phase relations of pyrolytic mantle composition as a function of depth. A high-spin to low-spin transition of iron in ferropericlase was reported by Badro et al. [61]. The phase transition Ca-perovskite from cubic to tetragonal structure was observed by Ono et al. [21]. The stability field of CaIrO_3 -type phase of Fe- and Al-bearing MgSiO_3 composition was determined in this study.

be orthorhombic Mg-perovskite, cubic Ca-perovskite, and ferropericlase. Recent DAC studies reported on the possibility of a phase transition of Ca-perovskite and ferropericlase. Using the precise angle-dispersive X-ray diffraction measurements, Shim et al. [60] found that pure CaSiO_3 perovskite has a tetragonal structure at room temperature. Ono et al. [21] observed that the cubic-tetragonal transition of Ca-perovskite in the peridotite composition occurred at high pressures and high temperatures, but the transition temperatures were much lower than those typical in the mantle geotherm. Therefore, this structural phase transition cannot occur in the lower mantle, and Ca-perovskite exhibits the cubic structure. Experiments indicate that a high-spin to low-spin transition in ferropericlase occurs at high pressures [61]. Badro et al. [61] reported this transition occurring at $P=60\text{--}70$ GPa, corresponding to a depth of 2000 km in the lower mantle. However, Badro et al.'s measurements were performed only at room temperature. It is therefore necessary to perform further studies to assess the occurrence of the high-spin to low-spin transition at high pressures and high temperatures corresponding to those of the actual lower mantle conditions. At the base of the lower mantle, cubic Ca-perovskite and ferropericlase remain stable. In contrast, orthorhombic Mg-perovskite transforms to the CaIrO_3 -type phase at the D'' layer, which causes

interesting features [27], such as seismic anisotropy [5], discontinuity [1,4], and an anticorrelation between the bulk and shear sound velocities [6,8]. Previous studies have reported on the decomposition of MgSiO_3 perovskite at pressures corresponding to those of the lower mantle [62,63]. However, recent theoretical and experimental studies suggest that the mixture of a two-oxide assemblage, MgO and SiO_2 , is not stable throughout the pressure-temperature regime of the lower mantle [e.g., [17,18,20,21,64]]. The decomposition of MgSiO_3 perovskite due to incongruent melting and the diffusion of MgSiO_3 perovskite in huge temperature gradient have been observed [65].

In the natural mantle composition, the orthorhombic Mg-perovskite and CaIrO_3 -type phases are not likely to have the pure MgSiO_3 composition. It is known that orthorhombic Mg-perovskite contains significant FeO, Fe_2O_3 , and Al_2O_3 components in the peridotite composition [e.g., [24,25,51,66,67]]. These components cause a shift in the phase boundary between the orthorhombic Mg-perovskite and the CaIrO_3 -type phase. Table 2 shows the difference in enthalpy between the reactions depicted in Eqs. (1a) and (1b) for some elements involved in these reactions. Surprisingly, we find that all divalent impurities, except for Fe^{2+} , are much more soluble in the perovskite phase. For Fe^{2+} doping, we found that in both

the perovskite and the CaIrO_3 -type structures, the high-spin Fe^{2+} configuration was more stable at 120 GPa than the low-spin configuration. This conclusion is important for mantle chemistry, and will be only reinforced by the inclusion of on-site electron correlations (using such methods as DFT+U) that were omitted in our pure density-functional treatment. The partition coefficients indicate that the incorporation of FeO into MgSiO_3 stabilizes the CaIrO_3 -type phase, while the opposite effect is seen for CaO. A recent theoretical study on the high-pressure phase of Al_2O_3 has interesting implications for the incorporation of Al_2O_3 in MgSiO_3 phases [68]. It was found that even though Al_2O_3 in the CaIrO_3 -type structure is more stable than in the orthorhombic perovskite structure above ~ 80 GPa, the Al_2O_3 component prefers to dissolve in the perovskite MgSiO_3 phase (see Table 2).

Fig. 8a shows schematic phase diagrams of the MgSiO_3 – Al_2O_3 system. The transition pressure increases as the Al_2O_3 component enters into the MgSiO_3 , because the Al_2O_3 content of the CaIrO_3 -type phase is lower than that of the coexisting perovskite phase. In contrast, the transition temperature decreases as the Al_2O_3 content increases. Fig. 8b shows phase diagrams of the MgSiO_3 – FeSiO_3 and MgSiO_3 – Fe_2O_3 systems. In these cases, the incorporation of iron components shows the opposite effect on the phase transition when compared to the MgSiO_3 – Al_2O_3 system. The CaIrO_3 -type structure in Fe_2O_3 is stable above 60 GPa (Table 6), and it has been reported that Fe_2O_3 components readily dissolve in the MgSiO_3 phase [24,25]. This evidence supports the incorporation of Fe_2O_3 resulting in the phase boundary of post-perovskite reaction shifted to lower pressures. According to the calculated partition coefficient of FeO (Table 1), the FeO component prefers to dissolve in the CaIrO_3 -type phase. The effect of incorporation of FeO is similar to that of Fe_2O_3 . It is difficult to predict the effect of all minor components on the phase boundary, however, because the incorporation of Al_2O_3 has an effect opposite to that of Fe_2O_3 and FeO. We determined the phase boundary between orthorhombic Mg-perovskite and the CaIrO_3 -type phase both in pure MgSiO_3 and for natural compositions. However, as we used different pressure standards (platinum or gold) in each experiment, it was difficult to assess the precise shift of this phase boundary, and consistency between different

pressure standards at high temperatures was not established, although it is recognized that a correct pressure scale is of fundamental importance for interpreting geophysical observations using laboratory experimental data obtained at high pressures and temperatures [53]. If it is assumed that there is no significant inconsistency between the platinum and gold pressure standards, then these impurities in natural rock systems are likely to cause a shift of several GPa in the phase boundary toward low pressures (Fig. 8c).

After the phase change to the CaIrO_3 -type phase assemblage has occurred, the mineral constitution will change. As the Al_2O_3 content in the MgSiO_3 phase will decrease when the phase change occurs, a certain concentration of this component will enter into the Ca-perovskite and ferropericlase phases. However, most of the Al_2O_3 will dissolve into the Ca-perovskite phase, because previous studies have shown that the Al_2O_3 content of ferropericlase is negligible [51,67]. Consequently, the mineral proportion of Ca-perovskite phase increases after the phase change (Fig. 7). In contrast, FeO and Fe_2O_3 prefer to enter into the CaIrO_3 -type phase when compared to the orthorhombic Mg-perovskite phase. The solubility of iron in Ca-perovskite is low [51,67]. Therefore, the mineral proportion of ferropericlase decreases slightly at the phase change. The change in density of the rock at the bottom of the lower mantle is due to the change in crystal structure of the MgSiO_3 phases, and also to the change in the mineral proportions according to the partition coefficients of aluminium and iron among the coexisting minerals.

Table 2 shows the physical properties of the CaIrO_3 -type phase. The third-order Birch–Murnaghan equation of state was used to describe the thermoelastic properties of the CaIrO_3 -type phase. The bulk modulus (K_{T0}) of the high-pressure phase was, usually, larger than that of the low-pressure phase. However, the bulk modulus of the CaIrO_3 -type phase was lower than that of the orthorhombic MgSiO_3 perovskite phase. The change in density between the orthorhombic Mg-perovskite and the CaIrO_3 -type phase bearing assemblage in the mantle composition was calculated. The estimated change in density at the phase change was 1.1% at 0 K. This change in density decreases as the temperature increases. A numerical study has reported that a dense layer generated from composi-

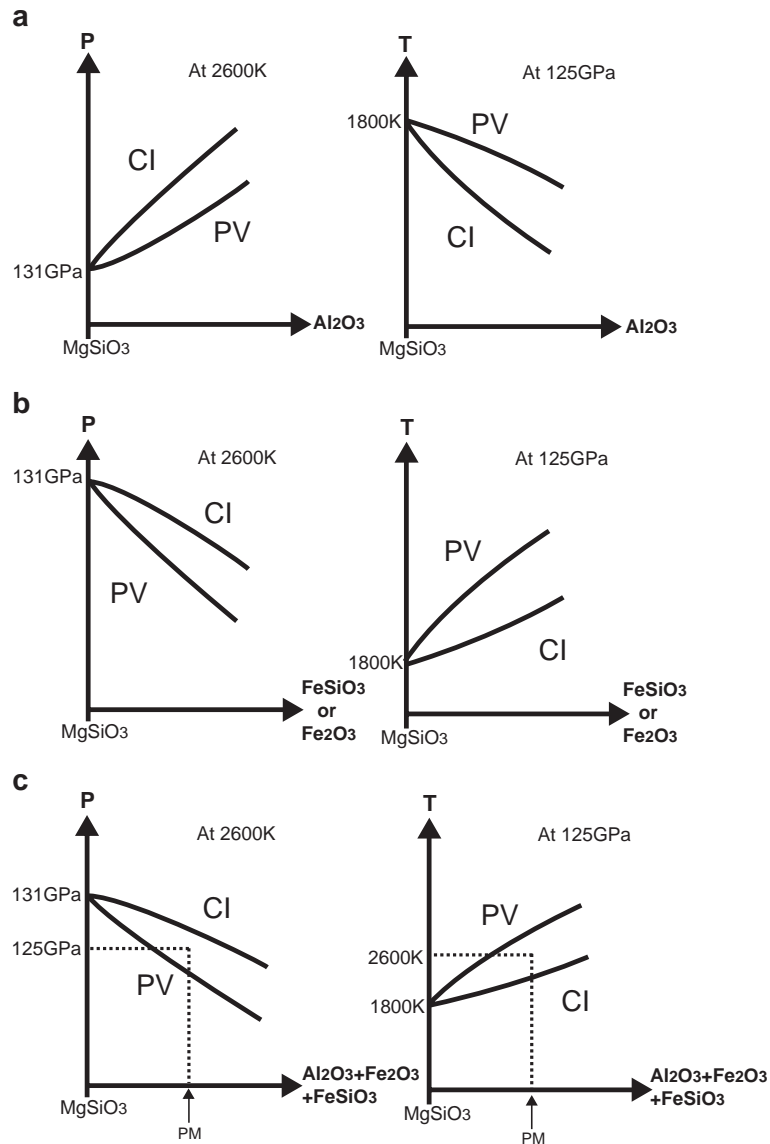


Fig. 8. Schematic phase diagram of $\text{MgSiO}_3\text{S} - \text{Al}_2\text{O}_3$, $\text{MgSiO}_3 - \text{FeSiO}_3$, $\text{MgSiO}_3 + \text{Fe}_2\text{O}_3$, and natural systems at 125 GPa and 2600 K. a, $\text{MgSiO}_3 - \text{Al}_2\text{O}_3$ system. b, $\text{MgSiO}_3 - \text{FeSiO}_3$ and $\text{MgSiO}_3 + \text{Fe}_2\text{O}_3$ systems. c, pyrolitic mantle composition. PM indicates the pyrolitic mantle composition. CI and PV represent CaIrO_3 -type and orthorhombic Mg-perovskite phase, respectively. A pressure and temperature condition of the phase change from orthorhombic Mg-perovskite to CaIrO_3 -type phase assemblages was determined in Fig. 5.

tional differentiation in the deep mantle is needed to explain the thermal history of the Earth [69]. According to our D'' layer model, however, such a dense layer could be formed by the above phase transition. The temperature difference from a transition from the orthorhombic Mg-perovskite to the CaIrO_3 -type phase bearing assemblage can be estimated using

the calculated thermodynamic properties [27], and is $\Delta T = 50$ K. Although the rheological properties of the CaIrO_3 -type phase are unknown, the increase in temperature at the phase change may contribute to a lower viscosity of the D'' layer. The viscosity of ferropericlase is lower than that of the orthorhombic perovskite phase and thus it will significantly affect

Table 6
Comparison of phase boundary between the orthorhombic perovskite and CaIrO_3 -type phases

	a (GPa)	b (MPa/K)	Pressure scale
MgSiO ₃			
Experiment ^a	130	7.0	Pt: Holmes et al. [47]
	126	6.7	Pt: Jamieson et al. [49]
Calculation ^b	122.6	9.56	GGA
	108.3	9.85	LDA
		8	Thermodynamic analysis
Fe ₂ O ₃			
Experiment ^c	62	2.2	
KLB-1 peridotite			
Experiment ^d	124	8	Au: Jamieson et al. [49]
Observation			
Seismic ^d	123 ^e	6	

The phase boundary is represented as P (GPa) = $a + b \times (T$ (K) – 2500).

^a This study.

^b Oganov and Ono [27].

^c Ono et al. [26].

^d Sidorin et al. [4].

^e Temperature at the top of the D' layer corresponding to 2700 km depth is assumed as 2500 K.

the deformation in the lower mantle [70]. If the diffusion creep of ferropericlase becomes dominant at the base of the lower mantle, then the decrease in viscosity is less than an order of magnitude as the mantle temperature increases during the phase transition [71]. It is known that diffusion creep is sensitive to the grain size of a mineral. If a reduction in grain size occurs during the phase change, then rheological softening may occur. In contrast, there is the possibility that the plastic flow properties in the D' layer are controlled by dislocation creep, which will be discussed later.

If we assume that the composition of the lower mantle is the KLB-1 peridotite [72], which has a similar composition to pyrolite, then the mantle temperature at a depth of 2700 km depth would be about 2600 K based on observations of the seismic discontinuity and the phase boundary determined in this study (Fig. 6). Ito and Katsura [73] reported that the mantle temperature at a depth of 660 km, which was determined using the same analogy, was about 1973 K. According to both estimations, the average adiabatic gradient of the lower mantle is 0.31 K/km (Table 2), which is consistent with the value from a thermal model calculated using thermo-elastic properties [74].

The phase transition from orthorhombic Mg-perovskite to the CaIrO_3 -type phase has a large Clapeyron slope of 7 and 8 MPa/K for pure MgSiO₃ and the pyrolitic mantle composition, respectively. When the mantle geotherm of the early Earth was much higher than that of the present Earth, the D' layer did not exist at the base of the lower mantle. Fig. 9 shows a schematic temperature profile of the early, present, and future Earth. After the magma ocean and core formation events, the temperature at the base of the lower mantle was outside the stability field of the CaIrO_3 -type bearing assemblage. Then, the D' layer appeared during the cooling of the Earth. Assuming one model of the thermal history of the Earth [75], the D' layer was formed ~200 Myr after the formation of the Earth. When the D' layer became composed of CaIrO_3 -type phase bearing rock, the temperature of the lowermost part of the mantle was too high for the CaIrO_3 -type phase to exist, since the temperature immediately near the CMB was more than 4000 K, and only the perovskite phase was stable (Fig. 9). Therefore, the CaIrO_3 -type phase bearing rock became wedged between orthorhombic Mg-perovskite bearing rocks (Fig. 10). Recent seismic investigations into the fine structure at the lowermost few hundreds km of the mantle have reported that two sharp changes occur in the seismic velocity [76]. First struc-

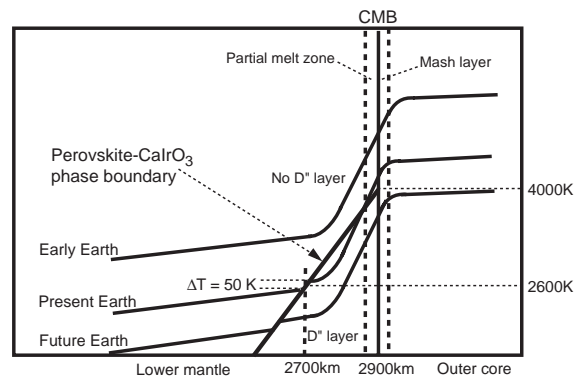


Fig. 9. Geotherms at the core–mantle boundary in the early and present Earth. Partial melt zone is corresponding to the ultra-low seismic velocity layer at the base of the lower mantle [91]. Mash layer consists of the liquid iron and the precipitated crystals [e.g., [92]]. Perovskite– CaIrO_3 phase boundary in pyrolitic mantle composition was determined in this study. A temperature change at the phase change was estimated by Oganov and Ono [27]. This figure indicates that the D' layer grows up during the Earth's history.

ture shows a sharp increase 200–300 km above the CMB. The second structure lies 55–85 km above the CMB, and is marked by a sharp reduction in velocity. These seismic structures seem to indicate that a sandwich structure presently exists in the Earth's mantle [77]. This sandwich structure will disappear in the

future, when the temperature of the CMB decreases to below 4000 K.

From the viewpoint of geochemistry, the formation of the D'' layer is significant. It is recognized that various geochemical heterogeneities, such as isotope elements, are observed in the mantle [78]. Most mantle heterogeneities have been reported from hot spots, which are likely to originate from the deep mantle. The circulation of subduction-related materials, oceanic crusts, and sediments, can lead to some geochemical heterogeneities [78,79]. However, the heterogeneity of the isotope of noble gases, e.g. the He^3/He^4 ratio, cannot be explained by subduction-related materials. Observations of high He^3/He^4 ratios indicates that primordial materials exist in the deep mantle [80,81]. Recently, several models have been proposed to explain the geochemical constraints on mantle structures, while simultaneously being consistent with the structure imaged using global seismic tomography models [82]. We propose a new model for the formation of the D'' layer that employs a primordial material source at the core–mantle boundary. Fig. 10 shows a schematic illustration of the core–mantle boundary in the early, present, and future Earth. During the magma ocean and core formation events, the lower mantle material was an orthorhombic Mg-perovskite bearing assemblage. Radioactive elements, which determine the isotope heterogeneities, were distributed according to the partition coefficients between the orthorhombic Mg-perovskite bearing rock and the iron melt. After the formation of the D'' layer, the radioactive elements were redistributed at the core–mantle boundary according to the partition coefficients between the CaIrO_3 -type phase bearing rock and the iron melt of the outer core. It is known that incompatible elements prefer to distribute into Ca-perovskite in

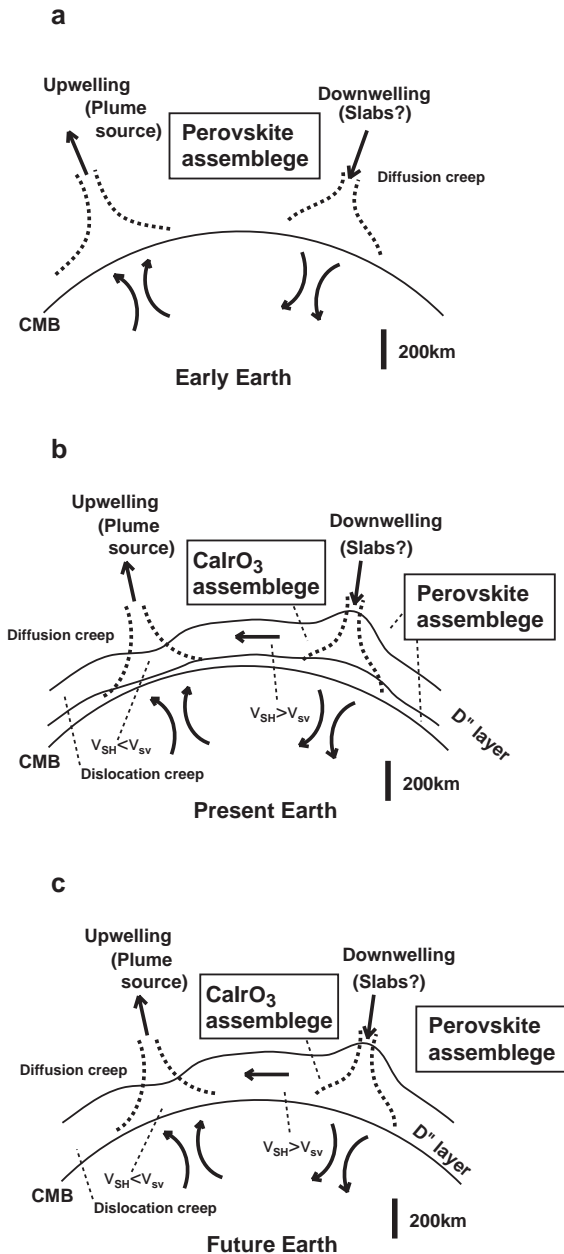


Fig. 10. Schematic illustration of the bottom of the mantle in the early, present, and future Earth. The D'' layer did not exist at just after the Earth formation, because the mantle temperature in the early Earth was much higher than that in the present Earth. The D'' layer is consist of the CaIrO_3 -type bearing assemblage. The temperature heterogeneity of the D'' layer causes the depth fluctuation of seismic discontinuity at the top of the D'' layer. V_{SH} and V_{SV} indicate horizontally and vertically polarized shear waves [5]. The seismic anisotropy shows a flow direction of mantle convection in the D'' layer. Thick arrows are flow directions at bottom of the lower mantle and the outer core. The creep mechanism of the mantle material changes from the diffusion creep to the dislocation creep at the boundary between the lower mantle and the D'' layer.

the lower mantle [83,84]. We expect a strong partitioning of many elements to occur between the perovskite and CaIrO_3 -type phases (see Table 1, showing this effect for divalent elements). Therefore, incompatible elements, including radioactive elements (e.g., K, U, and Th) would be redistributed between the mantle and core. The isotope character of CaIrO_3 -type phase bearing rocks will thus be different from that of orthorhombic Mg-perovskite bearing rocks. There is a possibility that the indicators from primordial materials, such as a high He^3/He^4 ratio, originate from a chemical interaction between the D'' layer and the outer core. Osmium isotope data from hot spots suggest the occurrence of a core–mantle interaction [85]. It is possible that the behaviour of the D'' layer composed of CaIrO_3 -type phase bearing rock contributes to the chemistry of hot spot magmas. As the smaller inner planets, such as Mercury and Mars, do not have a D'' layer, the geochemical signature of the magmas on these smaller planets are different from that of the Earth.

The D'' layer constituted by CaIrO_3 -type phase bearing rock plays an important role in the dynamics

of mantle convection and of the thermal history of the Earth. The phase transition from orthorhombic Mg-perovskite to CaIrO_3 -type phase exhibits a large Clapeyron slope. Therefore, in colder regions, where the subducted slabs descend into the D'' layer, the depth of the phase transition is much shallower than for normal geotherm regions. The differences in depth are 15 and 70 km for temperature changes of 100 and 500 K, respectively. Given that the amplitude of the topography of the D'' discontinuity is about 300 km (equivalent to 15 GPa), the present Clapeyron slope of 7 MPa/K implies a lateral temperature contrast of ~ 2100 K near the core–mantle boundary (or ~ 1600 K using the Clapeyron slope predicted by Oganov and Ono [27]). This coincides exactly with the estimate of ~ 2100 K obtained by Oganov et al. [40,41] using a completely different and independent method using seismic tomography maps and mineral–physics data. The thermal model [74] is shown in Fig. 11. Thus, the density of the colder region comprising the dense CaIrO_3 -type phase bearing rock becomes higher than that of the surrounding mantle. In contrast, the lower density in the hot region, where upwelling

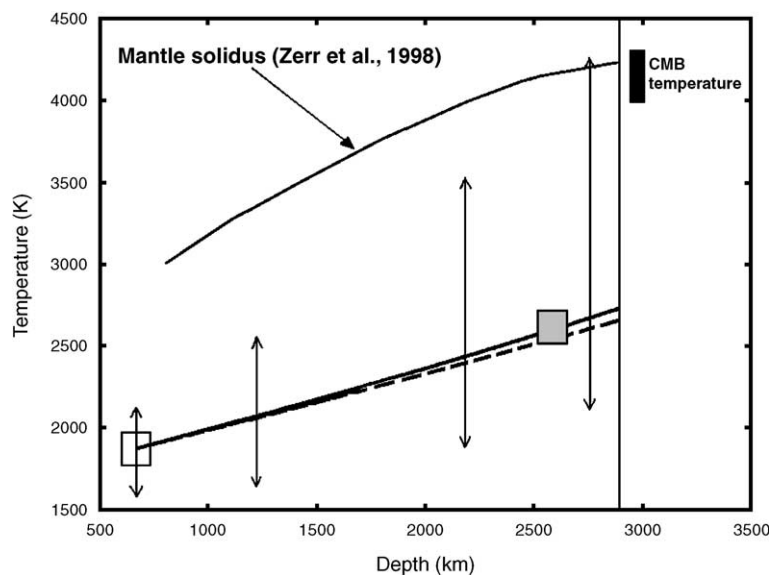


Fig. 11. Schematic temperature distribution in the lower mantle. Two-headed arrows indicate the maximum temperature contrasts (the lower and the upper arrows at each depth give the lowest and the highest temperature, respectively). Black and grey lines are adiabats calculated using Grüneisen parameters of MgSiO_3 and MgO , respectively: the difference is small, and the geotherm is well constrained between these lines. The temperature of the Earth's core at the boundary with the mantle [93] is indicated. This scheme implies partial melting of the lowermost mantle limited only to the hottest patches at the boundary with the core — in agreement with seismological evidence [94]. Melting temperature of the mantle rock was reported by Zerr et al. [95].

plumes exist, means the depth of the phase transition is much greater. These effects enhance convection at the base of the lower mantle. Moreover, the redistribution of radioactive elements in the D'' layer is significant from the geochemical perspective and also from the dynamics viewpoint. It is known that radioactive elements are an important internal heat source in the Earth. According to this behaviour, the D'' layer enable an efficient migration of heat from the core to the mantle. The efficiency of the cooling of the Earth was likely to have changed before and after the formation of the D'' layer. A recent numerical study on mantle convection including the phase transition from the orthorhombic Mg-perovskite to CaIrO₃-type phase supports these dynamical effects at the base of the mantle [86].

Seismic studies of the anisotropy in the D'' layer indicates the presence of active convection. The absence of seismic anisotropy in most of the lower mantle has led to the suggestion that diffusion creep is the dominant deformation mechanism [87], while anisotropy in the D'' layer indicates a transition in deformation mechanism from diffusion to dislocation creep. Dislocation creep follows a power-law function on shear stress, and leads to strongly preferred crystal orientation under large strains. The CaIrO₃-type phase exhibits a layered structure. If this forms a slip plane during deformation, then this slip plane may become oriented parallel to the convective flow. Many regions in the D'' layer show that horizontally polarized shear waves travel faster than the vertically polarised one ($V_{SH} > V_{SV}$) [e.g., 5]. The calculated anisotropy of this preferred crystal orientation is consistent with the observed seismic anisotropy [27]. This indicates that active horizontal flows exist in the D'' layer, the same as at top of the mantle. In contrast, a region where V_{SH} is lower than V_{SV} was observed under the Pacific Ocean. This seismic anisotropy indicates that a large vertical flow occurs under the Pacific Ocean at the bottom of the lower mantle. Seismic tomography images show that a large low-velocity region exists above the $V_{SH} < V_{SV}$ region in the lower mantle [88]. This decrease in seismic velocity, which is correlated with hot spots, seems to be associated with an increase in temperature [89,90]. Therefore, a large ascending plume under the Pacific Ocean originates from the D'' layer.

Acknowledgments

The synchrotron radiation experiments were performed at the BL10XU, SPring-8 (Proposal No. 2002A0106-ND-np 2002B0162-ND2-np, 2003A0013-LD2-np). We thank Y. Ohishi, M. Isshiki, N. Sata, T. Hanyu, T. Suzuki, and Y. Tatsumi for help in experiments. K. Mibe kindly provided us a sample of KLB-1 peridotite. Calculations were performed at CSCS (Manno) and ETH Zurich; we are grateful to A. Bernasconi and S. Mauri for help in calculations and to P.J. Tackley for discussions.

References

- [1] T. Lay, D.V. Helmberger, A shear velocity discontinuity in the lower mantle, *Geophys. Res. Lett.* 10 (1983) 63–66.
- [2] T. Lay, Q. Williams, E.J. Garnero, The core–mantle boundary layer and deep Earth dynamics, *Nature* 392 (1998) 461–468.
- [3] I. Sidorin, M. Gurnis, D.V. Helmberger, X. Ding, Interpreting D'' seismic structure using synthetic waveforms computed from dynamic models, *Earth Planet. Sci. Lett.* 163 (1998) 31–41.
- [4] I. Sidorin, M. Gurnis, D.V. Helmberger, Evidence for a ubiquitous seismic discontinuity at the base of the mantle, *Science* 286 (1999) 1326–1331.
- [5] M. Panning, B. Romanowicz, Inferences of flow at the base of Earth's mantle based on seismic anisotropy, *Science* 33 (2004) 351–353.
- [6] W.J. Su, A.M. Dziewonski, Simultaneous inversion for 3-D variations in shear and bulk velocity in the mantle, *Phys. Earth Planet. Inter.* 100 (1997) 135–156.
- [7] G. Masters, G. Laske, H. Bolton, A. Dziewonski, The relative behaviour of shear velocity, bulk sound velocity, bulk sound speed, and compressional velocity in the mantle: implications for chemical and thermal structure, in: S. Karato, A.M. Forte, R.C. Liebermann, G. Masters, L. Stixrude (Eds.), *Earth's Deep Interior: Mineral Physics and Tomography From the Atomic to the Global Scale*, AGU Geophysical Monograph, vol. 117, AGU, Washington D.C., 2000, pp. 63–87.
- [8] M. Ishii, J. Tromp, Normal-mode and free-air gravity constraints on lateral variations in velocity and density of Earth's mantle, *Science* 285 (1999) 1231–1236.
- [9] I. Sidorin, M. Gurnis, D.V. Helmberger, Dynamics of a phase change at the base of the mantle consistent with seismological observations, *J. Geophys. Res.* 104 (1999) 15005–15023.
- [10] M.E. Wyssession, A. Langenhorst, M.J. Fouch, K.M. Fischer, G.I. Al-Eqabi, P.J. Shore, T.J. Clarke, Lateral variations in compressional/shear velocities at the base of the mantle, *Science* 284 (1999) 120–125.
- [11] S. Rondenay, K. Fischer, Constraints on localized core–mantle boundary structure from multichannel, broadband SKS coda analysis, *J. Geophys. Res.* 108 (2003) 2537.

- [12] A.K. McNamara, P.E. van Keken, S. Karato, Development of finite strain in the convecting lower mantle and its implications for seismic anisotropy, *J. Geophys. Res.* 108 (2003) 2230.
- [13] P.J. Tackley, Strong heterogeneity caused by deep mantle layering, *Geochem. Geophys. Geosyst.* 3 (2002) 1024.
- [14] R. Holme, Electromagnetic core–mantle coupling: II. Probing deep mantle conductance, in: M. Gurnis, M.E. Wysession, E. Knittle, B.A. Buffert (Eds.), *The core–mantle boundary region*, AGU, 1998, pp. 139–151.
- [15] H. Nagao, T. Iyemori, T. Higuchi, T. Araki, Lower mantle conductivity anomalies estimated from geomagnetic jerks, *J. Geophys. Res.* 108 (2003) 2254.
- [16] E. Knittle, R. Jeanloz, Synthesis and equation of state of (Mg,Fe)SiO₃ perovskite to over 100 gigapascals, *Science* 235 (1987) 668–670.
- [17] G. Serghiou, A. Zerr, R. Boehler, (Mg,Fe)SiO₃-perovskite stability under lower mantle conditions, *Science* 280 (1998) 2093–2095.
- [18] S.E. Kesson, J.D. Fitz Gerald, J.M. Shelley, Mineralogy and dynamics of a pyrolite lower mantle, *Nature* 393 (1998) 252–255.
- [19] G. Fiquet, A. Dewaele, T. Le Bihan, Thermoelastic properties and crystal structure of MgSiO₃ perovskite at lower mantle pressure and temperature conditions, *Geophys. Res. Lett.* 27 (2000) 21–24.
- [20] D. Andrault, Evaluation of (Mg,Fe) partitioning between silicate perovskite and magnesiowüstite up to 120 GPa and 2300 K, *J. Geophys. Res.* 106 (2001) 2079–2088.
- [21] S. Ono, Y. Ohishi, K. Mibe, Phase transition of Ca-perovskite and stability of Al-bearing Mg-perovskite in the lower mantle, *Am. Mineral.* 89 (2004) 1480–1485.
- [22] M.J. Walter, A. Kubo, T. Yoshino, J. Brodholt, K.T. Koga, Y. Ohishi, Phase relations and equation-of-state of aluminous Mg-silicate perovskite and implications for Earth's lower mantle, *Earth Planet. Sci. Lett.* 222 (2004) 501–516.
- [23] S. Ono, T. Kikegawa, Y. Ohishi, High-pressure phase transition of hematite Fe₂O₃, *J. Phys. Chem. Solids* 65 (2004) 1527–1530.
- [24] C.A. McCammon, Perovskite as a possible sink for ferric iron in the lower mantle, *Nature* 384 (1997) 694–696.
- [25] D.J. Frost, C. Liebske, F. Langenhorst, C.A. McCammon, R.G. Trønnes, D. Rubie, Experimental evidence for the existence of iron-rich metal in the Earth's lower mantle, *Nature* 428 (2004) 409–412.
- [26] S. Ono, Y. Ohishi, In situ X-ray observations of phase transformation in Fe₂O₃ at high pressures and high temperatures, *J. Phys. Chem. Solids* (in press).
- [27] A.R. Oganov, S. Ono, Theoretical and experimental evidence for a post-perovskite phase of MgSiO₃ in Earth's D'' layer, *Nature* 430 (2004) 445–448.
- [28] T. Tsuchiya, J. Tsuchiya, K. Umemoto, R.M. Wentzcovitch, Phase transition in MgSiO₃ perovskite in the earth's lower mantle, *Earth Planet. Sci. Lett.* 224 (2004) 241–248.
- [29] M. Murakami, K. Hirose, K. Kawamura, N. Sata, Y. Ohishi, Post-perovskite phase transition in MgSiO₃, *Science* 304 (2004) 855–858.
- [30] S.H. Shim, T.S. Duffy, R. Jeanloz, G. Shen, Stability and crystal structure of MgSiO₃ perovskite to the core–mantle boundary, *Geophys. Res. Lett.* 31 (2004) L10603.
- [31] S. Ono, T. Kikegawa, Y. Ohishi, A high-pressure and high-temperature synthesis of platinum carbide, *Solid State Commun.* 133 (2005) 55–59.
- [32] S. Ono, Y. Ohishi, M. Isshiki, T. Watanuki, In situ X-ray observations of phase assemblages in peridotite and basalt compositions at lower mantle conditions, *J. Geophys. Res.* 110 (2005) B02208.
- [33] A.P. Hammersley, S.O. Svensson, M. Hanfland, A.N. Fitch, D. Häusermann, Two-dimensional detector software: from real detector to idealized image or two-theta scan, *High Press. Res.* 14 (1996) 235–245.
- [34] J.P. Perdew, K. Burke, M. Ernzerhof, Generalized gradient approximation made simple, *Phys. Rev. Lett.* 77 (1996) 3865–3868.
- [35] P.E. Blöchl, Projector augmented-wave method, *Phys. Rev., B* 50 (1994) 17953–17979.
- [36] G. Kresse, D. Joubert, From ultrasoft pseudopotentials to the projector augmented-wave method, *Phys. Rev., B* 59 (1999) 1758–1775.
- [37] G. Kresse, J. Furthmüller, Efficient iterative schemes for ab initio total-energy calculations using a plane wave basis set, *Phys. Rev., B* 54 (1996) 11169–11186.
- [38] S. Nosé, A molecular dynamics method for simulations in the canonical ensemble, *Mol. Phys.* 52 (1984) 255–268.
- [39] A.R. Oganov, P.I. Dorogokupets, All-electron pseudopotential study of MgO: equation of state, anharmonicity, and stability, *Phys. Rev., B* 67 (2003) 224110.
- [40] A.R. Oganov, J.P. Brodholt, G.D. Price, Ab initio elasticity and thermal equation of state of MgSiO₃ perovskite, *Earth Planet. Sci. Lett.* 184 (2001) 555–560.
- [41] A.R. Oganov, J.P. Brodholt, G.D. Price, The elastic constants of MgSiO₃ perovskite at pressures and temperatures of the Earth's mantle, *Nature* 411 (2001) 934–937.
- [42] L.V. Al'tshuler, S.E. Brusnikin, E.A. Kuzmenkov, Isotherms and Grüneisen functions of 25 metals, *J. Appl. Mech. Tech. Phys.* 161 (1987) 134–146.
- [43] V.S. Vorob'ev, On model description of the crystalline and liquid states, *Teplofiz. Vys. Temp. (High-Temperature Thermophysics)* 34 (1996) 397–406.
- [44] S.H. Shim, T. Duffy, G. Shen, Stability and structure of MgSiO₃ perovskite to 2300-kilometer depth in Earth's mantle, *Science* 293 (2001) 2437–2440.
- [45] H.K. Mao, R.J. Hemley, Y. Fei, J.F. Shu, L.C. Chen, A.P. Jephcoat, Y. Wu, W.A. Basset, Effect of pressure, temperature and composition on the lattice parameters and density of three (Fe,Mg)SiO₃ perovskite up to 30 GPa, *J. Geophys. Res.* 101 (1991) B8257–B8269.
- [46] J. Häglund, G. Grimvall, T. Jarlborg, A.F. Guillermet, Band structure and cohesive properties of 3d-transition-metal carbides and nitrides with the NaCl-type structure, *Phys. Rev., B* 43 (1991) 14400–14408.
- [47] N.C. Holmes, J.A. Moriarty, G.R. Gathers, W.J. Nellis, The equation of state of platinum to 660 GPa (6.6 Mbar), *J. Appl. Phys.* 66 (1989) 2962–2967.

- [48] T. Tsuchiya, K. Kawamura, First-principles electronic thermal pressure of metal Au and Pt, *Phys. Rev.*, B 66 (2002) 094115.
- [49] J.C. Jamieson, J.N. Fritz, M.H. Manghnani, Pressure measurement at high temperature in X-ray diffraction studies: gold as a primary standard, in: S. Akimoto, M.H. Manghnani (Eds.), *High-Pressure Research in Geophysics*, Center for Academic Publishing, Tokyo, 1982, pp. 27–48.
- [50] T. Irifune, A.E. Ringwood, Phase transitions in primitive MORB and pyrolite compositions to 25 GPa and some geophysical implications, in: M.H. Manghnani, Y. Syono (Eds.), *High-pressure Research in Mineral Physics*, Terra Scientific Publishing Company, Tokyo/American Geophysical Union, Washington, D.C. (1987) pp. 231–242.
- [51] N. Nishiyama, T. Irifune, T. Inoue, J. Ando, K. Funakoshi, Precise determination of phase relations in pyrolite across the 660 km seismic discontinuity by in situ X-ray diffraction and quench experiments, *Phys. Earth Planet. Inter.* 143–144 (2004) 185–199.
- [52] S. Ono, T. Katsura, E. Ito, M. Kanzaki, A. Yoneda, M.J. Walter, S. Urakawa, W. Utsumi, K. Funakoshi, In situ observation of ilmenite–perovskite phase transition in MgSiO₃ using synchrotron radiation, *Geophys. Res. Lett.* 28 (2001) 835–838.
- [53] Y. Fei, J. Li, K. Hirose, W. Minarik, J.V. Orman, C. Sanloup, W. van Westrenen, T. Komabayashi, K. Funakoshi, A critical evaluation of pressure scales at high temperatures by in situ X-ray diffraction measurements, *Phys. Earth Planet. Inter.* 143–144 (2004) 515–526.
- [54] O.L. Anderson, D.G. Isaak, S. Yamamoto, Anharmonicity and the equation of state for gold, *J. Appl. Phys.* 65 (1989) 1534–1543.
- [55] S.H. Shim, T.S. Duffy, K. Takemura, Equation of state of gold and its application to the phase boundaries near 660 km depth in Earth's mantle, *Earth Planet. Sci. Lett.* 203 (2002) 729–739.
- [56] T. Tsuchiya, First-principles prediction of the P–V–T equation of state of gold and the 660-km discontinuity in Earth's mantle, *J. Geophys. Res.* 108 (2003) 2462.
- [57] D.L. Heinz, R. Jeanloz, The equation of state of the gold calibration standard, *J. Appl. Phys.* 55 (1984) 885–893.
- [58] T. Katsura, H. Yamada, O. Nishikawa, M. Song, A. Kubo, T. Shinmei, S. Yokoshi, Y. Aizawa, T. Yoshino, M.J. Walter, E. Ito, Olivine–wadsleyite transition in the system (Mg Fe)₂SiO₄, *J. Geophys. Res.* 109 (2004) B02209.
- [59] E. Ito, E. Takahashi, Postspinel transitions in the system Mg₂SiO₄–Fe₂SiO₄ and some geophysical implications, *J. Geophys. Res.* 94 (1989) 10637–10646.
- [60] S.H. Shim, R. Jeanloz, T.S. Duffy, Tetragonal structure of CaSiO₃ perovskite above 20-GPa, *Geophys. Res. Lett.* 29 (2002) 2166.
- [61] J. Badro, G. Fiquet, F. Guyot, J.P. Rueff, V.V. Struzhkin, G. Vankó, G. Monaco, Iron partitioning in Earth's mantle: toward a deep lower mantle discontinuity, *Science* 300 (2003) 789–791.
- [62] C. Meade, H.K. Mao, J. Hu, High-temperature phase transition and dissociation of (Mg Fe)SiO₃ perovskite at lower mantle pressures, *Science* 268 (1995) 1743–1745.
- [63] S.K. Saxena, L.S. Dubrovinsky, P. Lazor, Y. Cerenius, P. Häggkvist, M. Hanfland, J. Hu, Stability of perovskite (MgSiO₃) in the Earth's mantle, *Science* 274 (1996) 1357–1359.
- [64] A.R. Oganov, G.D. Price, Ab initio thermodynamics of MgSiO₃ perovskite at high pressures and temperatures, *J. Chem. Phys.* 122 (2005) 124501.
- [65] H.K. Mao, G. Shen, R.J. Hemley, Multivariable dependence of Fe–Mg partitioning in the lower mantle, *Science* 278 (1997) 2098–2100.
- [66] B.J. Wood, D.C. Rubie, The effect of alumina on phase transformations at the 660-kilometer discontinuity from Fe–Mg partitioning experiments, *Nature* 273 (1996) 1522–1524.
- [67] B.J. Wood, Phase transformations and partitioning relations in peridotite under lower mantle conditions, *Earth Planet. Sci. Lett.* 174 (2000) 341–354.
- [68] A.R. Oganov, S. Ono, New phase of alumina (Al₂O₃) at high pressures and temperatures. *Proc. Natl. Acad. Sci.* (in press).
- [69] T. Nakagawa, P.J. Tackley, Effects of thermo-chemical mantle convection on the thermal evolution of the Earth's core, *Earth Planet. Sci. Lett.* 220 (2004) 107–119.
- [70] P. Li, S. Karato, Z. Wang, High-temperature creep in fine-grained polycrystalline CaTiO₃, an analogue material of (Mg,Fe)SiO₃ perovskite, *Phys. Earth Planet. Inter.* 95 (1996) 19–36.
- [71] J. Ita, E. Cohen, Diffusion in MgO at high pressures: implications for lower mantle rheology, *Geophys. Res. Lett.* 25 (1998) 1095–1098.
- [72] S. Ono, T. Kikegawa, T. Iizuka, The equation of state of orthorhombic perovskite in a pyrolitic mantle to 80 GPa: implications for chemical composition of the lower mantle, *Phys. Earth Planet. Inter.* 145 (2004) 9–17.
- [73] E. Ito, T. Katsura, A temperature profile of the mantle transition zone, *Geophys. Res. Lett.* 16 (1989) 425–428.
- [74] A.R. Oganov, J.P. Brodholt, G.D. Price, Ab initio theory of thermoelasticity and phase transitions in minerals, in: C.M. Gramaccioli (Ed.), *Energy Modelling in Minerals*, EMU Notes in Mineralogy, vol. 4, Eötvös University Press, Budapest, 2002, pp. 83–170.
- [75] F. Nimmo, G.D. Price, J.P. Brodholt, D. Gubbins, The influence of potassium on core and geodynamo evolution, *Geophys. J. Int.* 156 (2004) 363–376.
- [76] C. Thomas, F.M. Kendall, J. Lowman, Lower-mantle seismic discontinuities and the thermal morphology of subducted slabs, *Earth Planet. Sci. Lett.* 225 (2004) 105–113.
- [77] J.W. Hernlund, C. Thomas, P.J. Tackley, A doubling of the post-perovskite phase boundary and structure of the Earth's lowermost mantle, *Nature* 434 (2005) 882–886.
- [78] A.W. Hofmann, Mantle geochemistry: the message from oceanic volcanism, *Nature* 385 (1997) 219–229.
- [79] T. Hanyu, I. Kaneoka, The uniform and low ³He/⁴He ratios of HIMU basalts as evidence for their origin as recycled materials, *Nature* 390 (1997) 273–276.
- [80] I. Kaneoka, Noble gas constraints on the layered structure of the mantle, *Nature* 302 (1983) 698–700.
- [81] K.A. Farley, E. Neroda, Noble gases in the Earth's mantle, *Annu. Rev. Earth Planet. Sci.* 26 (1998) 189–218.

- [82] P.J. Tackley, Mantle convection and plate tectonics: toward an integrated physical and chemical theory, *Science* 288 (2000) 2002–2007.
- [83] T. Kato, A.E. Ringwood, T. Irifune, Experimental determination of element partitioning between silicate perovskites, garnets, and liquids: constraints on early differentiation of the mantle, *Earth Planet. Sci. Lett.* 89 (1988) 123–145.
- [84] A. Corgne, B.J. Wood, CaSiO₃ and CaTiO₃ perovskite-melt partitioning of trace elements: implications for gross mantle differentiation, *Geophys. Res. Lett.* 29 (2002) 1933.
- [85] A.D. Brandon, R.J. Walker, J.W. Morgan, M.D. Norman, H.M. Prichard, Coupled ¹⁸⁶Os and ¹⁸⁷Os evidence for core–mantle interaction, *Science* 280 (1998) 1570–1573.
- [86] T. Nakagawa, P.J. Tackley, Effects of a perovskite–post perovskite phase change near core–mantle boundary in compressible mantle convection, *Geophys. Res. Lett.* 31 (2004) L16611.
- [87] S. Karato, S. Zhang, H. Wenk, Superplasticity in Earth’s lower mantle: evidence from seismic anisotropy and rock physics, *Science* 270 (1995) 458–461.
- [88] D. Zhao, Seismic structure and origin of hot spots and mantle plumes, *Earth Planet. Sci. Lett.* 192 (2001) 251–265.
- [89] M.A. Richards, B.H. Hager, N.H. Sleep, Dynamically supported geoid highs over hotspots: observation and theory, *J. Geophys. Res.* 93 (1998) 7690–7708.
- [90] M.S. Thorne, E.J. Garnero, S.P. Grand, Geographic correlation between hot spots and deep mantle lateral shear-wave velocity gradients, *Phys. Earth Planet. Inter.* 146 (2004) 47–63.
- [91] T. Lay, E.J. Garnero, Q. Williams, Partial melting in a thermochemical boundary layer at the base of the lower mantle, *Phys. Earth Planet. Inter.* 146 (2004) 441–467.
- [92] B.A. Buffett, E.J. Garnero, R. Jeanloz, Sediments at the top of Earth’s core, *Science* 290 (2000) 1338–1342.
- [93] D. Alfè, M.J. Gillan, L. Vočadlo, J. Brodholt, G.D. Price, The ab initio simulation of the Earth’s core, *Philos. Trans. R. Soc. Lond. Ser. A* 360 (2002) 1227–1244.
- [94] Q. Williams, E. Garnero, Seismic evidence for partial melt at the base of Earth’s mantle, *Science* 273 (1996) 1528–1530.
- [95] A. Zerr, A. Diegler, R. Boehler, Solidus of Earth’s deep mantle, *Science* 281 (1998) 243–246.